Advance Access publication 2025 October 25

Downloaded from https://academic.oup.com/mnras/article/544/2/1903/8301217 by guest on 27 November 2025

Detection of quasi-periodic oscillations in the γ -ray light curve of 4FGL J0309.9-6058

Jingyu Wu[®],¹ Zhihao Ouyang[®],¹ Hubing Xiao[®],¹★ Elisa Prandini[®],² Shangchun Xie,¹ Sheng Yang[®],³ Jianzhen Chen, ^{1★} Shaohua Zhang ¹⁰, ¹ Haoyang Zhang ¹⁰⁴ and Junhui Fan ^{105,6,7}

Accepted 2025 October 20. Received 2025 September 30; in original form 2025 April 21

ABSTRACT

In this work, we report, for the first time, a quasi-periodic oscillation (QPO) in the γ -ray band of 4FGL J0309.9–6058, also known as PKS 0308-611. We employed three analytical methods (the Lomb-Scargle periodogram, REDFIT, and the weighted wavelet Z-transform) to analyse the QPO signal using Fermi γ -ray light curve data. The analysis reveals a potential QPO during MJD 57983–60503, with a period of approximately 550 d and a maximum local significance of 3.72σ and global significance of 2.72σ derived from the WWZ analysis. To validate this result, we applied Gaussian Process (GP) to the same light curve, which independently confirms the presence of QPO signal consistent with our Fourier-based results. We further extended the analysis to the full duration of the Fermi observations, and the results consistently support and strengthen the presence of this QPO signal. Additionally, a time lag between the optical and γ -ray bands indicates separate emission regions for these two bands. Given the year-like time-scale of the QPO signal and the fact that a QPO signal with local significance over 3σ for full Fermi-LAT observed time, we suggest that the QPO is most likely caused by a precessing jet.

Key words: galaxies: active – galaxies: jets – quasars: individual: 4FGL J0309.9–6058.

1 INTRODUCTION

Active galactic nuclei (AGNs) are luminous central regions of a small fraction of galaxies, emitting more radiation than their host galaxies. The extraordinary brightness is due to the energy released as matter within the accretion disc loses angular momentum and gravitational potential energy and falls into the centre supermassive black hole (SMBH; E. E. Salpeter 1964; D. Lynden-Bell 1969; C. M. Urry & P. Padovani 1995). AGNs can be broadly classified into jet-type and non-jet-type categories based on the presence of their jets (P. Padovani 2017).

Blazars represent a distinctive class of AGN, characterized by their radio-loud property and relativistic jets pointed towards the observer. This unique orientation results in extreme properties, including rapid variability and strong emission across the entire electromagnetic spectrum, from radio bands to high-energy γ -rays. The spectral energy distribution (SED) of blazars typically exhibits a doublepeaked structure: the low-energy component, which spans from radio to X-ray wavelengths, is produced by synchrotron radiation of relativistic electrons, while the high-energy component, which

extends from X-ray to γ -ray bands, is generated by inverse Compton scattering of soft photons or through hadronic processes (R. D. Blandford & A. Koenigl 1979; A. Mücke & R. J. Protheroe 2001; G. Ghisellini & F. Tavecchio 2009; A. A. Abdo et al. 2010; J. H. Fan et al. 2016; G. G. Wang, J. T. Cai & J. H. Fan 2022; H.-B. Xiao et al. 2024; Z. Ouyang et al. 2025).

Quasi-periodic oscillations (QPOs) are used to study the emission mechanisms of blazars. They have been detected across a wide range of time-scales in different bands. The most famous example is the BL Lac object OJ 287, which exhibits a QPO in the optical band with a period of approximately 12 yr based on over a century of monitoring (A. Sillanpaa et al. 1988; M. J. Valtonen et al. 2006; J.-H. Fan et al. 2010). In addition, sources such as 1ES 1959+650, 3C 66A, B2 1633+38, 1823+568, 3C 454.3, 3C 273 have been reported QPO signals in the optical band (K. J. Schramm et al. 1993; J. H. Fan et al. 2014, 2018; J. Otero-Santos et al. 2020; F.-T. Dong et al. 2022; H.-Z. Li et al. 2022). Some sources have observed QPO signals in the X-ray and radio bands, such as PKS 0607-157 and 3C 454.3 (S.-J. Qian et al. 2007; X.-P. Li et al. 2023) The launch of the Large Area Telescope (LAT) aboard the Fermi Gamma-ray Space Telescope in 2008 has significantly enhanced the capability to conduct all-sky monitoring across various time-scales (W. B. Atwood et al. 2009) and provided the possibility of discovering QPOs in the γ -ray band. The

¹Shanghai Key Lab for Astrophysics, Shanghai Normal University, Shanghai 200234, P. R.China

²INFN, Università di Padova, I-35131 Padova, Italy

³Institute for Gravitational Wave Astronomy, Henan Academy of Sciences, Zhengzhou 450046, Henan, China

⁴Department of Astronomy, Key Laboratory of Astroparticle Physics of Yunnan Province, Yunnan University, Kunming 650091, P. R. China

⁵Center for Astrophysics, Guangzhou University, Guangzhou 510006, P. R. China

⁶Key Laboratory for Astronomical Observation and Technology of Guangzhou, Guangzhou 510006, P. R. China

⁷Astronomy Science and Technology Research Laboratory of Department of Education of Guangdong Province, Guangzhou 510006, P. R. China

^{*} E-mail: hubing.xiao@shnu.edu.cn (HX); jzchen@shnu.edu.cn (JC)

first QPO source in the γ -ray band was observed in PG 1553+113, which showed a period of about 2 yr (M. Ackermann et al. 2015). Based on over 16 yr of LAT data, more than 30 QPO signals in the γ -ray band were reported in blazars with periods ranging from months to years (e.g. A. Sandrinelli et al. 2016; D. A. Prokhorov & A. Moraghan 2017; P.-f. Zhang et al. 2017; G. Bhatta 2019; H. Zhang et al. 2021; H. Zhang, F. Wu & B. Dai 2023). There are many physical mechanisms that explain the phenomenon of QPO, such as binary SMBH systems (H. J. Lehto & M. J. Valtonen 1996; M. Villata et al. 1998), plasma blob helically moving forward along the jet (M. Camenzind & M. Krockenberger 1992), jet precession (Z. Abraham & E. A. Carrara 1998; Z. Abraham & G. E. Romero 1999), magnetic reconnection events within the jet (e.g. C.-Y. Huang et al. 2013), and hotspots on the accretion disc revolving around the black hole (S. K. Chakrabarti & P. J. Wiita 1993; A. V. Mangalam & P. J. Wiita 1993).

We searched for the QPO signals for each blazar in the *Fermi*-LAT Light Curve Repository (LCR) catalogue using the Lomb–Scargle Periodogram (LSP) method and found a significant QPO signal in 4FGL J0309.9–6058. Thus, in this work, we report a QPO signal of the distant flat-spectrum radio quasar (FSRQ) object 4FGL J0309.9-6058 (z=1.479) in the γ -ray band. And in this paper, we use the flat Lambda cold dark matter (Λ CDM) model with $H_0=67.66$ km Mpc⁻¹ s⁻¹ and $\Omega_{\rm M}=0.31$ (Planck Collaboration VI 2020). This paper is arranged as follows: we present the observation and data processing in Section 2; we show the analysis and results of QPO in Section 3; we provide the discussion and conclusions in Sections 4 and 5.

2 FERMI-LAT DATA REDUCTION

We collected the LAT data events from the Fermi-LAT Pass 8 data base within a 15° radius region of interest (ROI) centred on 4FGL J0309.9-6058. The data span from MJD 54683 to MJD 60443 and covers an energy range of 0.1-300 GeV. The data analysis was conducted using the latest FERMITOOLS (v2.2.0; Fermi Science Support Development Team 2019) and the instrument response functions (IRFs) P8R3_SOURCE_V3. The maximum zenith angle value of 90° was selected to avoid the background γ-rays from the Earth's limb. The condition 'evclass=128, evtvpe=3' was used to filter events with a high probability of being photons, and '(DATA_QUAL≥0)&& (LAT_CONFIG==1)' was used to select the good time intervals. The model file, generated by make4FGLxml PYTHON package, included all the sources from the Fermi-LAT Fourth Source Catalog (4FGL-DR4; S. Abdollahi et al. 2022) within 20° of the target source, as well as the Galactic (gll_iem_v07.fits) and extragalactic isotropic (iso_P8R3_SOURCE_V3_v1.txt) diffuse emission components. The normalization parameters and spectral indices of the sources within 5° of the target, as well as those of the sources within the ROI with a variability index (VI) ≥ 24.725 (S. Abdollahi et al. 2022), were set as free parameters. We checked through the likelihood analysis results, assuming a power-law model, and compared it with a log-parabola model. The result of test statistic for curve spectrum $TS_{curve} = -2(\log \mathcal{L}_{PL} - \log \mathcal{L}_{LP}) < 9$ showed that the log-parabola model is not significantly preferred over the power-law model, where \mathcal{L}_{PL} and \mathcal{L}_{LP} represent the maximum likelihood values obtained from a power law and a log-parabola fits (S. Abdollahi et al. 2020). Consequently, the target source spectrum is best described by the power-law model, which was used to generate the 30-d binned light curve using the binned likelihood method. We used the test statistic $TS = -2(\log \mathcal{L}_{nosource} - \log \mathcal{L}_{source})$ to calculate the significance of this source ($\mathcal{L}_{source/nosource}$ represents the likelihood of the data given the model with or without a source present at a given position). We included only flux data points significantly detected with TS \geqslant 9, while the 95 percent confidence level upper limit flux values were calculated using the UpperLimits¹ PYTHON tool for cases where TS < 9. The light curve is shown in panel (a) of Fig. 1.

3 QUASI-PERIODIC OSCILLATION ANALYSIS AND RESULTS

With visual inspection, we found a possible periodic variability during the campaign of MJD 57983–60503. In order to identify the existence of a QPO signal and to quantify the period, we employed the LSP, REDFIT, and weighted wavelet *Z*-transform (WWZ).

3.1 Lomb-Scargle periodogram analysis

LSP (N. R. Lomb 1976; J. D. Scargle 1982) is a widely used method for analysing periodic signals in time series data. The advantage of LSP is that it can handle non-uniformly sampled data, unlike the traditional Fourier transform. For irregular sampling, the LSP method iteratively fits sinusoidal curves with different frequencies to light curves and constructs the periodogram according to the goodness of fit, and can provide accurate frequency and power spectrum intensities. We computed the LSP power using the lombscargle² class provided by ASTROPY and setting the frequency range of $f_{\min} = \frac{1}{T}$ to $f_{\max} = \frac{N}{2T}$ (which corresponds to the Nyquist frequency f_{Nyq} , T represents the total period of observation) with a step of 0.00015, and also considered the flux uncertainties in the analysis. The LSP power indicates a prominent peak at the timescale of 561.29 d, with its uncertainty estimated from the full width at half-maximum (FWHM) of the Gaussian function fitted to the peak, as shown in panel (c) of Fig. 1. To assess the influence of the time sampling on the periodogram, particularly the presence of upper limits in the light curve which were treated as non-detections and excluded from the periodic analysis, we constructed a synthetic light curve by assigning constant flux values to the observed time sampling. The LSP of this sampling pattern (the so-called spectral window function) shows no significant peaks at or near the period identified in the analysis, confirming that the detected QPO (P = 561.29 d) is intrinsic to the source variability rather than an artefact of the sampling pattern. We used the false-alarm probability (FAP) to evaluate the confidence level of the LSP peak, whose functional form is as follows: $FAP(P_n) = 1 - (1 - prob(P > P_n))^M$, where the independent trials M is defined by $M = T \Delta f$ with $\Delta f = f_{
m Nyq} - f_{
m min}.$ The FAP denotes the probability that at least one of the M independent power values in a given frequency band of the white noise periodogram is greater than or equal to the power threshold P_n (J. H. Horne & S. L. Baliunas 1986). R. V. Baluev (2008) have given the method 'baluev', which employs extreme value statistics to compute an upper bound of the FAP for the aliasfree case. So we used the 'baluev' method to determine the falsealarm level (FAL) at a 99.99 per cent FAP, which shows in panel (c) of Fig. 1 with horizontal solid line, indicating that there is only a 0.01 per cent chance of observing such a high peak under the null hypothesis that the data contains no periodic signal.

¹https://fermi.gsfc.nasa.gov/ssc/data/analysis/scitools/upper_limits.html

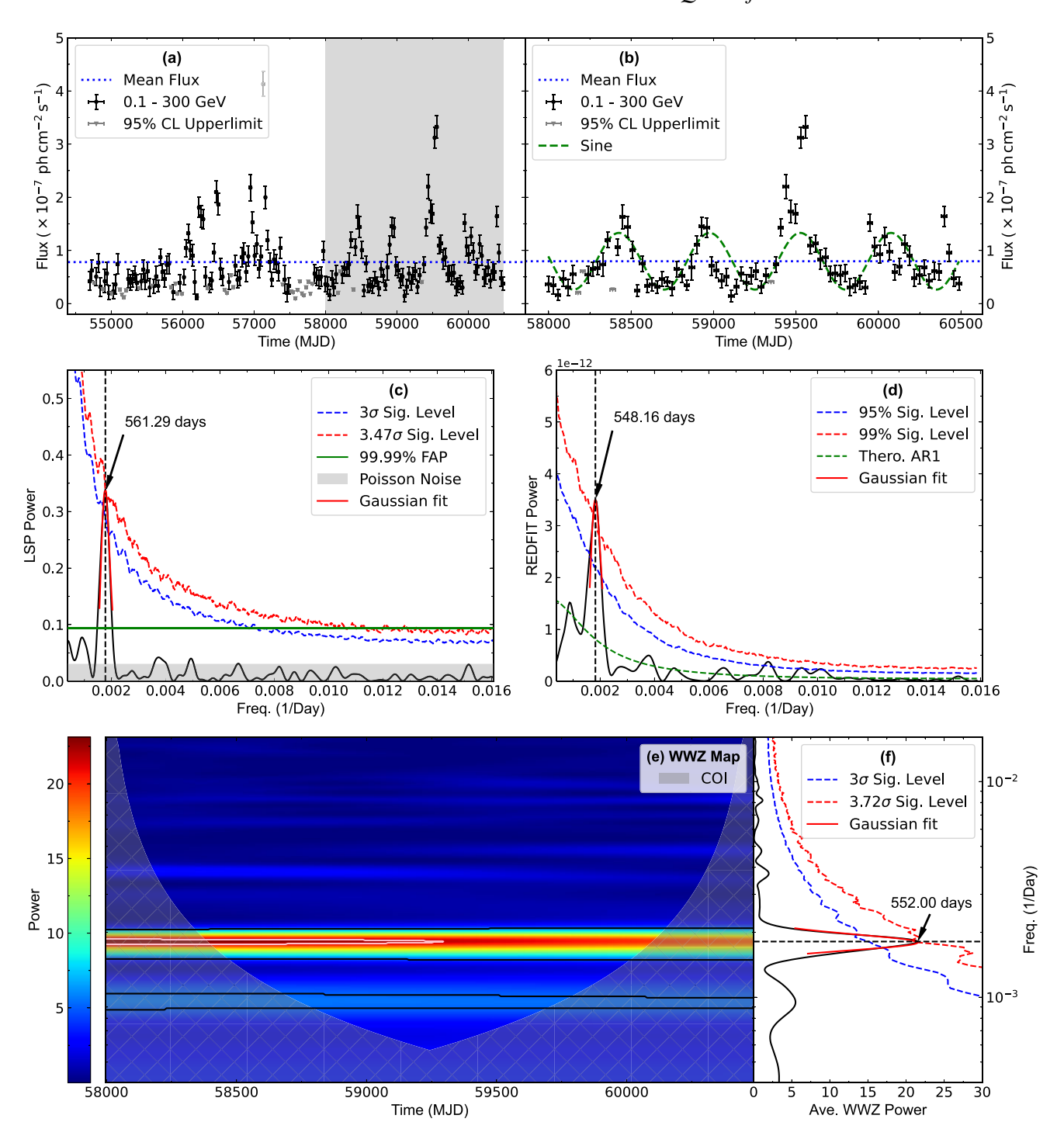


Figure 1. Panel (a): The Fermi-LAT light curve of 4FGL J0309.9–6056 for \sim 16 yr (MJD 54683–60503). The downward-pointing triangles represent the 95 percent significance level upper limits. Panel (b): The shaded section (MJD 57983–60503) from the left panel is enlarged. The dotted horizontal line represents the mean flux, and the solid line shows a sine function with a mean period of approximately 550 d derived from LSP, REDFIT, and WWZ methods. Panel (c): The LSP results for the period MJD 57983–60503 with peak value of 561.29 ± 74.15 d. The dotted curves represent the 3.00σ and 3.47σ local significance levels. The horizontal solid line indicates the 99.99 percent false-alarm probability, and the solid curve is the Gaussian function fitted to the peak. Furthermore, the Poisson noise level is calculated to be \sim 0.031 and is indicated by a shaded band. Panel (d): Results of the periodicity analysis by the REDFIT programme with a peak at 548.16 ± 83.04 d for the period MJD 57983–60503. The solid curve is the PSD calculated by REDFIT, the dashed curves represents the 99 percent significance levels by estimating the red noise background, and the theoretical AR1 spectrum. The solid curve is the Gaussian function fitted to the peak. Panel (e): The WWZ power spectrum map for the period MJD 57983–60503. The shaded region marks the cone of influence (COI). Panel (f): The solid curve shows the time-averaged WWZ. Dashed curves represent the 3.00σ local significance levels and the 3.72σ , which passes the peak value of 552.00 ± 65.66 d. A solid curve shows the Gaussian function fitted to the peak.

3.2 REDFIT

The light curves of AGNs are mainly affected by red noise, which results from some stochastic processes in a jet plasma or the accretion disc (X.-P. Li et al. 2017). For the non-uniform sampled data, it is difficult to accurately estimate the red-noise spectrum. REDFIT (M. Schulz & M. Mudelsee 2002) was developed to address this issue by directly fitting a first-order autoregressive (AR1) process to unevenly spaced time-series data, thus avoiding interpolation in the time domain and its inherent biases. As the emission fluxes of AGN are usually autoregressive (M. Schulz & M. Mudelsee 2002), we can use the AR1 process to model the emission red-noise spectrum. The programme REDFIT3.8E³ can estimate the spectrum using LSP and Welch overlapped segment averaging (WOSA). We set the oversampling factor for LSP (ofac) to 10, the number of WOSA segments ($n_{50} = 1$), and selected the Welch spectral window to reduce spectral leakage. The REDFIT provides a maximum significance level at FAP of 99 per cent corresponding to confidence levels of 2.58σ , which is estimated from the power spectrum against the red-noise background in the AR1 process (M. Schulz & M. Mudelsee 2002). As shown in panel (d) of Fig. 1, a distinct peak emerges at a time-scale of 548.16 d with a significance level exceeding 99 per cent. The periodicity uncertainty is estimated from the FWHM of the Gaussian function fitted to the REDFIT peak.

3.3 Weighted wavelet Z-transform analysis

The WWZ (G. Foster 1996) can transform data into the time domain and frequency domain and convolute the light curve with the kernel related to time and frequency. It can get the power intensity of periodic feature to search the periodicity by decomposing the signal into the frequency time space, and study its duration period. The Morlet kernel is defined as

$$f(\omega(t-\tau)) = e^{i\omega(t-\tau) - c\omega^2(t-\tau)^2},\tag{1}$$

where ω is the angular frequency, τ is the time translation parameter, and c is the window decay rate. Then, the WWZ power is given by

$$W[\omega, \tau; x(t)] = \omega^{1/2} \int x(t) f^*[\omega(t - \tau)] dt, \qquad (2)$$

where the f^* is the complex conjugate of the Morlet kernel f and x(t) is the light curve. More information concerning the WWZ method can be found in G. Foster (1996). We used a WWZ analysis PYTHON package⁴ to obtain the colour map of the WWZ power spectrum and the average power in a function of frequency. We set the frequency range of of $f_{\min} = \frac{1}{T}$ to $f_{\max} = \frac{N}{2T}$ with a step of 0.00015 and used c = 0.001. We also calculated the cone of influence (COI) to account for edge effects arising from the finite length of the data. The COI marks the region of the wavelet power spectrum where edge effects become significant and the results are less reliable. The results are shown in panels (e) and (f) of Fig. 1, and the time-average WWZ power gives the peak at 552.00 d. The corresponding periodicity uncertainty is estimated from the FWHM of the Gaussian function fitted to the peak.

3.4 Significance estimation

As mentioned above, we employed three methods to analyse QPO signals. However, the light curves of most AGNs exhibit frequencydependent red-noise characteristics, where both random flares and sampling instability can lead to the appearance of red noise, potentially generating false QPO signals. To quantify the significance of the observed periodicity detected by the LSP and WWZ methods, we applied the method developed by D. Emmanoulopoulos, I. M. McHardy & I. E. Papadakis (2013), which builds upon the approach by J. Timmer & M. König (1995). This method relies on the same properties of power spectral density (PSD) and probability distribution function (PDF) for the original light curve. Subsequently, the PYTHON code DELCGEN (S. D. Connolly 2016) was used to generate 10⁵ simulated light curves, which were then resampled to match the observational sampling, allowing us to assess the significance of the periodicity. The statistical significance derived from this procedure represents the local significance, which quantifies the significance level of the peak of the detected period at this specific period. However, without prior knowledge of the location of the peaks, it is more robust to check for a 'global significance'. Given that the search spans a wide range of frequencies, the possibility of detecting a spurious peak increases, which is also known as the 'look-elsewhere effect' or 'multiple comparison problem' in statistics (M. E. Bell et al. 2011). Therefore, the global significance estimates the significance of observing such a significant peak at any frequency within the search range, without prior knowledge of the peak location.

We used the power-law model $P(f) \propto f^{-\beta} + P_{\text{noise}}$ to effectively model the red-noise PSD of the original light curve (P. Uttley, I. M. McHardy & I. E. Papadakis 2002), where $\beta > 0$ is the power-law spectral slope, and P_{noise} represents the Poisson noise contribution. The Poisson noise is defined as

$$P_{\text{noise}} = \frac{2T}{N^2 u^2} \overline{F_{\text{err}}^2},\tag{3}$$

where N is the total number of measurements, μ is the mean flux, T is the total period of observation, and $\overline{F_{\rm err}^2}$ is the mean square of the flux uncertainties. We estimate the power-law spectral slope using the power spectral response method (PSRESP) method, which provides the 'success fraction' as a measurement of the goodness of fit (P. Uttley et al. 2002; R. Chatterjee et al. 2008; W. Max-Moerbeck et al. 2014). In this method, a total of M=1000 artificial light curves with red-noise characteristics were generated for each trial power-law slope β , ranging from 0.5 to 2.5 in steps of 0.1, using the Monte Carlo approach with J. Timmer & M. König (1995). Each simulated light curve was then resampled to match the observational sampling and processed to compute its PSD in the same way as the observed data. The PSRESP method evaluates how well the assumed PSD model reproduces the observed PSD by comparing the distribution of simulated PSDs with the observed one using a χ^2 -like function, which is defined as

$$\chi_{\text{obs}}^2 = \sum_{\nu = \nu_{\text{min}}}^{\nu_{\text{max}}} \frac{(\text{PSD}_{\text{obs}} - \overline{\text{PSD}}_{\text{sim}})^2}{(\Delta \text{PSD}_{\text{sim}})^2},\tag{4}$$

and

$$\chi_{\text{dist},i}^2 = \sum_{\nu = \nu_{\text{min}}}^{\nu_{\text{max}}} \frac{(\text{PSD}_{\text{sim},i} - \overline{\text{PSD}}_{\text{sim}})^2}{(\Delta \text{PSD}_{\text{sim}})^2},$$
 (5)

where $\overline{\text{PSD}}_{\text{sim}}$ is the average of $\text{PSD}_{\text{sim},i}$ and $\Delta \text{PSD}_{\text{sim}}$ is the standard deviation of $\text{PSD}_{\text{sim},i}$. The 'success fraction' is then determined by $\frac{m}{M}$ of the searching trial slopes, where m is the count of the number of $\chi^2_{\text{dist},i}$ for which χ^2_{obs} is smaller than $\chi^2_{\text{dist},i}$. The power-law slope

³https://www.marum.de/Prof.-Dr.-michael-schulz/Michael-Schulz-Software.html

⁴https://github.com/skiehl/wwz

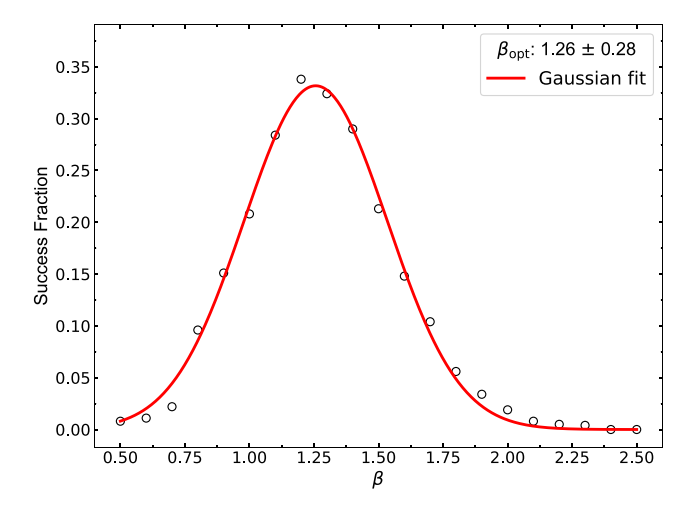


Figure 2. Power-law slope distribution as obtained using the PSRESP method. The best-fitting value of β_{opt} is obtained from the peak of a Gaussian function fit, and its associated uncertainty is taken from the FWHM of the Gaussian.

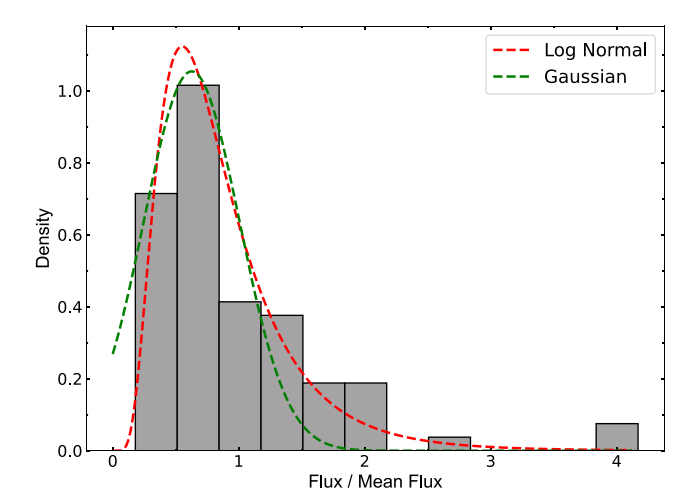


Figure 3. Histogram of γ -ray light curves for 4FGL J0309.9–6056. A dashed curve represents the log-normal fit, and another dashed curve represents the Gaussian fit.

Table 1. Fitting parameters for flux distributions of Fig. 3. RSS is the residual sum of squares.

	μ	σ	RSS
Gaussian	0.63	0.38	1.62
Log-normal	-0.29	0.55	1.18

distribution is shown in Fig. 2, giving a reliable estimate of the intrinsic spectral slope as $\beta_{opt}=1.26\pm0.28$. This value corresponds to the peak of a Gaussian function fitted to the distribution, with the associated uncertainty derived from the FWHM of the Gaussian. The PDF was conducted from the flux distribution histogram, as shown in Fig. 3. The fitting flux distribution parameters for Gaussian and lognormal are listed in Table 1. The Shapiro–Wilk statistics were applied to assess whether the original light curve originated from a Gaussian or a log-normal distribution (S. S. Shapiro & M. B. Wilk 1965). The

Shapiro-Wilk p-values are 1.86×10^{-9} and 0.45 for linear-scale and log-scale distribution tests, respectively, indicating flux distribution follows the log-normal distribution. The presence of a log-normal flux distribution suggests that the variability is driven by a non-linear multiplicative mechanism. In AGNs, such a distribution is often linked to fluctuations propagating through the accretion disc, where perturbations in the mass accretion rate multiply as they propagate inward, leading to a log-normal distribution of the flux (P. Uttley, I. M. McHardy & S. Vaughan 2005). In the case of blazars, where γ -ray variability is primarily associated with non-thermal radiation from the jet, the log-normal distribution may reflect multiplicative perturbations originating in the accretion disc and subsequently propagating into the jet. Additionally, γ -ray variability in blazars could arise from variations in jet instabilities, magnetic fields, particle densities, or seed photon fields, all of which can contribute to the lognormal flux distribution (G. Bhatta & N. Dhital 2020).

Finally, the local significance of the periodicity was estimated from the percentile distributions of the LSP and WWZ power at each frequency, derived from the 10^5 simulated light curves. The dashed curves in Fig. 1 represent the local significance levels of the LSP and WWZ methods. Furthermore, we estimated the global significance of the LSP and WWZ peaks using the approach described in S. O'Neill et al. (2022). As a result, we identified a periodic signal of 561.29 ± 74.15 d with a local significance of 3.47σ and a global significance of 2.30σ using the LSP method, a signal of 548.15 ± 83.04 d exceeding a 99 per cent significance level using REDFIT, and a signal of 552.00 ± 65.66 d with a local significance of 3.72σ and a global significance of 2.72σ based on the average WWZ power. All three methods consistently detected a QPO with a period of approximately 550 d in the γ -ray band, which corresponds to the mean value derived from these methods.

3.5 Gaussian Process modelling

The three methods used above, LSP, WWZ, and REDFIT, all analyse periodicity in the frequency domain. Gaussian Process (GP) modelling treats the observed variability as a realization of a stochastic process and allows for flexible modeling of correlated noise and intrinsic variations, which can be used to analyse periodicity in the time domain.

To model the light curve, we construct a GP composed of a sum of two stochastically driven damped harmonic oscillator (SHO) terms, each capturing variability on different time-scales. Each SHO term is described by the stochastic differential equation

$$\left[\frac{d^2}{dt^2} + \frac{\omega_0}{O}\frac{d}{dt} + \omega_0^2\right]y(t) = \epsilon(t),\tag{6}$$

where ω_0 is the undamped natural frequency, Q is the quality factor (which controls the sharpness of the resonance), and $\epsilon(t)$ is a white noise process. The corresponding power spectral density is given as

$$S(\omega) = \sqrt{\frac{2}{\pi}} \frac{S_0 \omega_0^4}{\left(\omega^2 - \omega_0^2\right)^2 + \omega^2 \omega_0^2 / Q^2},\tag{7}$$

where S_0 is the power normalization.

We use the CELERITE⁵ package (D. Foreman-Mackey et al. 2017) to construct the light curve variability, in which the parameters are expressed in the natural logarithmic space. Parameter estimation is carried out using Markov chain Monte Carlo (MCMC) with EMCEE

⁵https://celerite.readthedocs.io/en/stable/

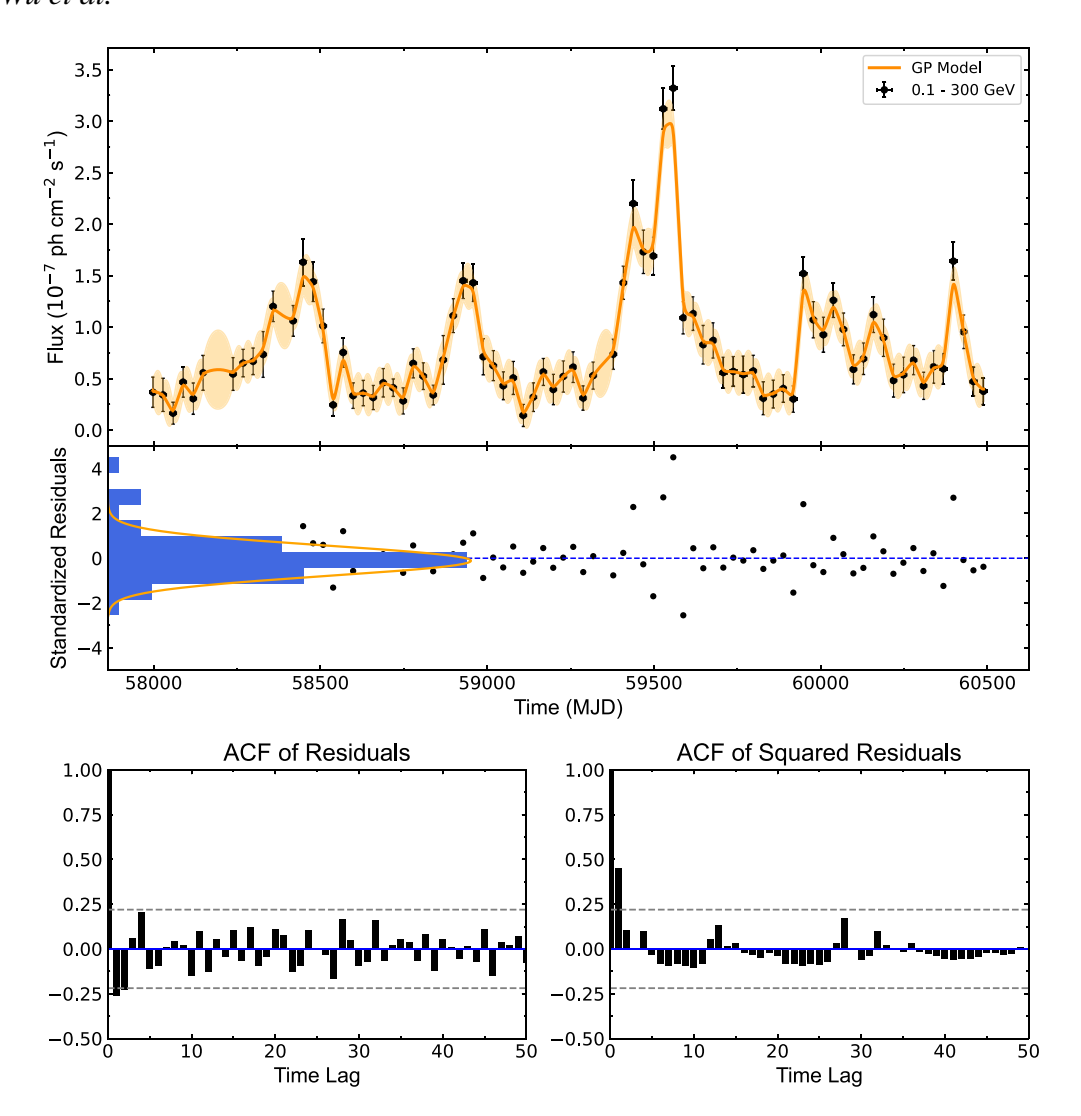


Figure 4. Gaussian Process modelling of the 0.1–300 GeV γ -ray light curve for the period MJD 57983–60503, obtained using the SHO \times 2 model. Top panel: Observed data and the best-fitting profile including the 1σ confidence interval. Middle panel: Standardized residuals of the Gaussian Process fit as a function of time. Bottom panels: Autocorrelation function (ACF) of the residuals (left) and squared residuals (right).

Table 2. Parameters of Gaussian Process modelling.

Model	ln S ₀	ln Q	$\ln \omega_0$
SHO × 2	$2.83^{+0.95}_{-1.31}$	$-1.37^{+0.80}_{-0.79}$	$-2.85^{+0.52}_{-0.40}$
	$-0.35^{+2.50}_{-2.84}$	$0.88^{+2.44}_{-2.89}$	$-4.49^{+0.23}_{-0.23}$
Prior	(-5, 5)	(-5, 5)	(-5, -2)

sampler, generating $32 \times 20\,000$ samples and discarding the initial 32×2000 as burn-in. The remaining samples are then used to derive the posterior estimates. The modelled light curve and the fitted values of model parameters are presented in Fig. 4 and Table 2, respectively. The posterior distributions for the model parameters are shown in Fig. A1. Additionally, the PSD of the model is shown in Fig. 5. And it shows a peak at the frequency of ~ 0.00178 d $^{-1}$ (561.79 d).

Residual analysis using the Shapiro–Wilk test confirms that the residuals are consistent with normality (p=0.26), suggesting the model effectively accounts for the intrinsic variability. Moreover, the autocorrelation function (ACF) and squared ACF of the residuals remain within the 95 per cent confidence interval, suggesting that the

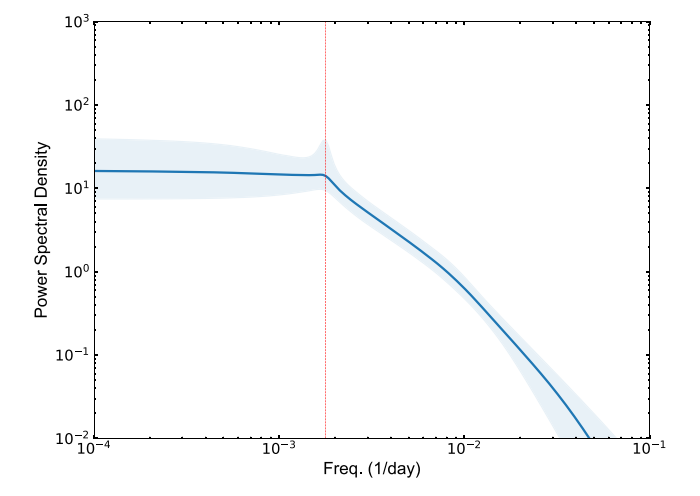


Figure 5. Power spectral density of the Gaussian Process modelling obtained using the SHO \times 2 model. The shaded regions correspond to 1σ confidence interval.

Table 3. Detected periods from different methods.

Method	Period	Local significance	Global significance
Lomb–Scargle Periodogram (LSP)	561.29 ± 74.15	3.47σ	2.30σ
Weighted Wavelet Z-transform (WWZ)	552.00 ± 65.66	3.72σ	2.72σ
REDFIT	548.16 ± 83.04	_	_
Gaussian Process	$561.79_{-129.20}^{+130.54}$	-	_

model successfully captures the temporal correlation structure in the

As a result, the GP modelling also revealed a period consistent with the QPO period of \sim 550 d identified by the Fourier-based methods. The detailed results obtained from each method are summarized in Table 3.

4 DISCUSSION

Building upon the findings in the previous section, both Fourier-based methods and GP modelling consistently identified a QPO with a characteristic timescale of approximately 550 d.

4.1 Extended analysis throughout the entire duration

We extended our search to cover the entire time span of *Fermi*-LAT observations and applied the LSP method to analyse the periodicity over MJD 54683–60503. As shown in Fig. 6, a periodic signal with a time-scale of approximately 600 d is detected, with a local significance exceeding 3σ and a global significance of 2.49σ . We also perform the WWZ analysis for the entire duration to examine the time localization of approximately 600-d QPO with a significance exceeding 3σ and a global significance of 2.24σ . The result confirms that this periodic signal exists nearly in the full period, as shown in panels (c) and (d) of Fig. 6. These significances were estimated following the approach as described in Section 3.4. This result is consistent with previous findings, but now confirmed over a longer observational baseline.

4.2 Time lag between optical and gamma-ray band

We also extended our search to other wavelengths and found that the Asteroid Terrestrial-impact Last Alert System (ATLAS) observation contributed to this investigation. After data collection, automated image processing was performed, including photometric and astrometric calibration using the RefCat2 reference catalogue (J. L. Tonry et al. 2018a, b). A reference image was then subtracted to identify transient events. Detected sources in the difference images were filtered through a transient discovery pipeline (the ATLAS Transient Server; K. W. Smith et al. 2020). For this study, we queried the ATLAS forced photometry service for data spanning from MJD 59 577 to 60625. We plotted the ATLAS data together with the γ ray data and the sine function in panel (a) of Fig. 7. We noticed that the optical ATLAS data appear to coincide with the predicted γ -ray sine function in the range of MJD 59800–60400, and this coincidence suggests that the QPO signal may also appear in the optical band, although we lack sufficient optical data to perform a detailed periodic analysis. Given the similarity in flux variation between the γ -ray and optical bands in panel (a) of Fig. 7, we analysed the cross-correlation between the γ -ray and optical flux using discrete correlation function (DCF; R. A. Edelson & J. H.

Krolik 1988) with the MUTIS⁶ package. During the DCF analysis, the optical data were binned into 1-d intervals, and the γ -ray data were binned into 5-d intervals. Note that a shorter time interval of the γ -ray light curve can reveal more detailed DCF structures, but this comes with increased flux errors and reduced TS values, which can decrease the quality of the DCF result. A compromised 5-d interval γ -ray light curve data were chosen to avoid numerous upper limit data points, which could significantly reduce the quality of the DCF result and obtain a trustable DCF result. The statistical significances and the uncertainties of the DCF correlation were estimated using a Monte Carlo approach by generating N = 2000 synthetic light curves for each signal. The generation process used the Lomb-Scargle to compute the PSD and the non-uniform Fourier transform to reconstruct the signals with similar PSD, mean, and standard deviation. Detailed information can be found in the description of MUTIS. The 8-d DCF bin size is used to calculate the DCF correlation, which is presented in panel (b) of Fig. 7, showing a time-lag of -228 d with 3.5σ . We also tested the different DCF bin sizes of 10, 12, 15, and 20, finding a consistent \sim 220-d time lag with significance levels of 1.9σ , 2.5σ , 3.2σ , and 3.2σ , respectively. The time lag between optical and γ -ray band is very likely to exist, and this lag provides valuable constraints for QPO models.

In the model of jet helical structure, the blob helically moving forward along the jet could cause a periodically changing viewing angle, Doppler factor, and further flux variation. On one hand, this model usually yields a QPO time-scale range from a few days to months, and these blobs are likely generated during flares and last for only a short time-scale (F. M. Rieger 2004; B. Rani, P. J. Wiita & A. C. Gupta 2009; J. Zhou et al. 2018; A. Banerjee et al. 2023; J. Chen et al. 2024). On the other hand, we found an optical- γ -ray time lag suggesting separated emission regions for these two bands, and in conflict with the single moving blob in the helical jet model. Unless we assume a complicated helical model of two separated blobs simultaneously moving in the jet. Thus, this model is less promising for interpreting the QPO signal in this work. In the following, we focus on the binary SMBH system and the precession of the relativistic jet.

4.3 Binary supermassive black hole system

The binary SMBH system assumes that the centre of the galaxy consists of two SMBHs, providing an important framework for explaining the QPO phenomenon. There are two different explanations: *lighthouse model* (M. Villata et al. 1998; S.-J. Qian et al. 2007) and *accretion model* (H. J. Lehto & M. J. Valtonen 1996; M. J. Valtonen et al. 2006; S.-J. Qian et al. 2007; J. H. Fan et al. 2014). In the framework of *lighthouse model*, M. Villata et al. (1998) suggested that both black holes in the binary system generate relativistic jets that are bent significantly in different directions. In the course of

⁶https://mutis.readthedocs.io/en/latest/

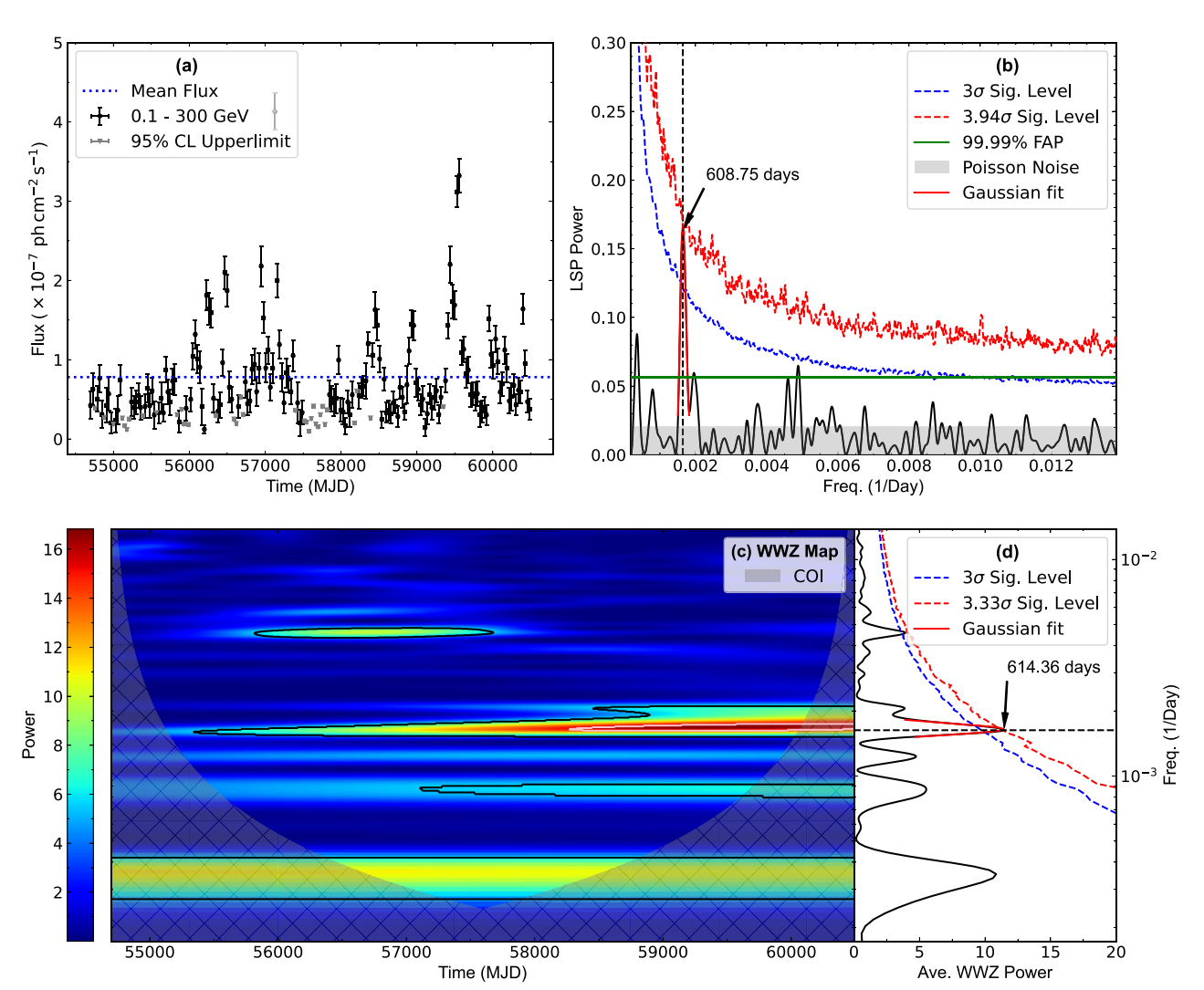


Figure 6. Panel (a): γ -ray LC for the entire time of *Fermi*-LAT observations (MJD 54683-60503). A dotted horizontal line indicates the mean flux. Panel (b): The LSP results for MJD 54683-60503. There is a peak at 608.75 ± 42.60 d with more than 3σ local significance. The other labels are the same as Fig. 1. Panels (c) and (d) show the WWZ power spectrum map and the time-averaged WWZ power for the period MJD 54683-60503. A significant peak is observed at 614.36 ± 54.74 d, exceeding the 3σ local significance level.

the binary's orbit motion, the directions of the bent parts of the jets from the two black holes rotate with the orbital period, resulting in periodic double-peak flares. If so, the γ -ray light curve would exhibit a distinct double-peak feature. However, we do not observe a clear double-peak feature [see panel (a) of Fig. 1]. Thus, this model is less likely to explain the QPO signal in this work.

Accretion model is that the secondary black hole crossing the accretion disc of the primary black hole can increase the accretion rate. For the binary supermassive black system, the total mass of the binary is $M_{\rm tot}=M_{\rm p}+M_{\rm s}$, where $M_{\rm p}$ is the mass of the primary BH and $M_{\rm s}$ is the mass of the secondary BH. The orbital period of the binary P can be calculated by Kepler's law

$$(a_1 + a_2)^3 = \frac{GM_{\text{tot}}}{4\pi^2} P^2, \tag{8}$$

where a_1 and a_2 are semimajor axes. It can be equivalent to the following (e.g. J. H. Fan et al. 2014, 2021)

$$P \sim 1.72 M_8^{-1/2} r_{16}^{3/2} \left(1 + \frac{M_s}{M_p} \right)^{-1/2} \text{yr.}$$
 (9)

The M_8 is the primary black hole mass in units of $10^8 \, \rm M_\odot$ and $r_{16} = a_1 + a_2$ is in units of 10^{16} cm. And the P can be calculated by observed period $P_{\rm obs}$ as

$$P = \frac{P_{\text{obs}}}{1+z}.\tag{10}$$

Taking $M_{\rm p}=10^{8.87}{\rm M}_{\odot}$ (M. S. Shaw et al. 2012), $\frac{M_{\rm s}}{M_{\rm p}}\sim 0.001$ and the observed period 550 d, we obtain $r_{16}=1.044$ (3.383 mpc). The orbiting and merger of the binary SMBH would generate a stochastic nHz GW background (A. Sesana 2013). For the case of our source, we expect the gravitational waves at $f=2/P_{\rm obs}\sim 42.1$ nHz. For a quasi-circular orbit, the gravitational waves strain is given by (M. Maggiore 2007)

$$h = \frac{2(GM_{\oplus})^{5/3}(\pi f)^{2/3}}{c^4 D},\tag{11}$$

where the luminosity distance of this source is 11.00 Gpc and the observed-frame chirp mass is

$$M_{\oplus} = \frac{(1+z)(M_s M_p)^{3/5}}{(M_s + M_p)^{1/5}}.$$
 (12)

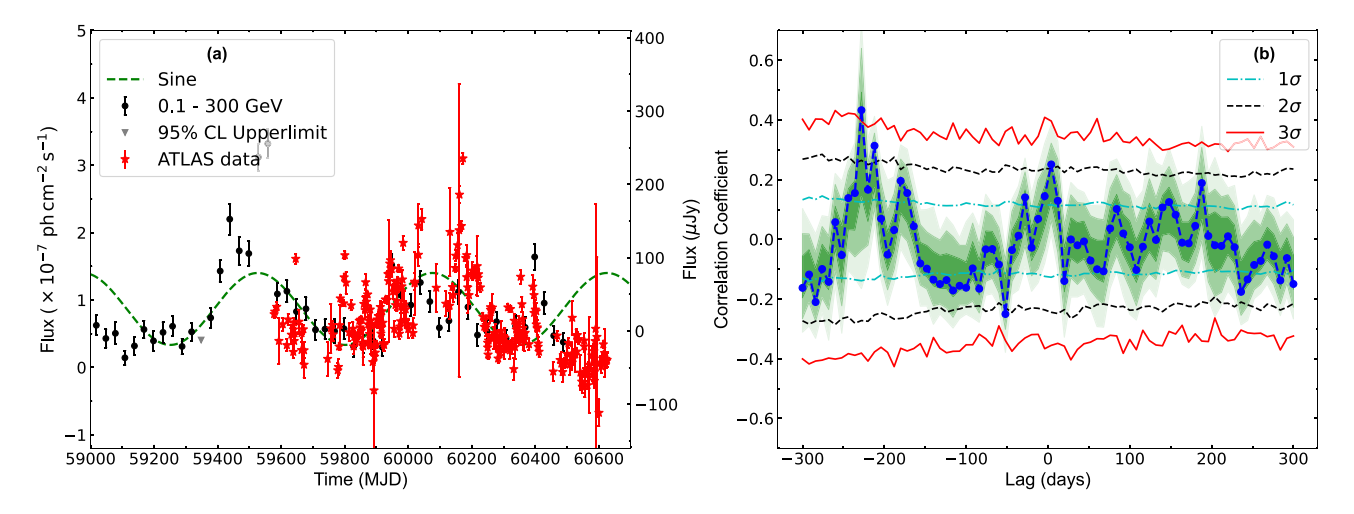


Figure 7. Panel (a): The optical-band light curve of this source is shown together with the quasi-simultaneous gamma-ray light curve. The optical light curve was binned at 1-d intervals. For the γ -ray data, a 30-d binning was used for visualization here, while a 5-d binning was adopted specifically for the DCF analysis. The sinusoidal curve is the same as that derived from panel (b) of Fig. 1. Panel (b): The result of cross-correlation between γ -ray and optical bands with a bin size of 8 d; similar results are obtained for other bin sizes. Reference curves indicate the 1.0, 2.0, and 3.0 σ significance levels. The peak at –228 d indicated that the optical band is ahead of the γ -ray band.

We can get the gravitational waves strain $h = 1.8 \times 10^{-19}$. Current gravitational wave detectors Laser Interferometer Gravitational-Wave Observatory (LIGO) (10 Hz-10 kHz; LIGO Scientific Collaboration 2015) and Virgo (10 Hz-up to a few kHz; T. Accadia et al. 2012) cannot detect gravitational waves in this frequency. Currently, the Pulsar Timing Array (PTA) is the only known effective method to detect GWs in the nHz band. There are several major PTAs: Parkes Pulsar Timing Array (PPTA; C. Bassa et al. 2008), North American Nanohertz Observatory for Gravitational Waves (NANOGrav; F. Jenet et al. 2009), Chinese Pulsar Timing Array (CPTA; K. J. Lee 2016; H. Xu et al. 2023), South Africa Pulsar Timing Array (SAPTA; R. Spiewak et al. 2022), European Pulsar Timing Array (EPTA; A. Chalumeau et al. 2022), and International Pulsar Timing Array (IPTA; R. N. Manchester & IPTA 2013). Specifically, based on the 15-yr data set of NANOGrav (G. Agazie et al. 2023a), the sensitivity of NANOGrav ($h \sim 10^{-14}$; G. Agazie et al. 2023b) is not enough for the gravitational waves strain of this source.

We propose that it may be possible to distinguish binary black hole systems on a geometric scale. The broad-line region (BLR) luminosity ($L_{\rm BLR}$) can be calculated using the following equation:

$$L_{\rm BLR} = L_{\rm line} \frac{\langle L_{\rm BLR} \rangle}{L_{\rm line,frac}},\tag{13}$$

where $L_{\rm line}$ denotes the emission-line luminosity and $L_{\rm line,frac}$ represents the luminosity ratio. The luminosity ratios utilized are 77, 22, 34, and 63 for H α , H β , Mg II, and C IV (A. Celotti, P. Padovani & G. Ghisellini 1997). Using the data from M. S. Shaw et al. (2012), we calculated the BLR luminosity log $L_{\rm BLR}=44.88~{\rm erg~s^{-1}}$. Assuming BLR covering factor is 0.1, we got the accretion disc luminosity log $L_{\rm disc}$ as 45.88 erg s⁻¹. The size of the BLR ($R_{\rm BLR}$), calculated by the equation $R_{\rm BLR}=10^{17}L_{\rm disc,45}^{1/2}=2.75\times10^{17}~{\rm cm}$ (G. Ghisellini & F. Tavecchio 2008; L. Zhang et al. 2024). Compared to r_{16} , the size of the BLR is larger than the separation between the binary black holes, making it challenging to distinguish the binary black holes using the optical spectrum. Consequently, confirming the binary black hole systems through optical observations remains extremely challenging.

4.4 Jet precession

The jet precession model emerges as the most promising explanation. The precessing jet generates QPO signals in both the optical and γ -ray bands and the observed time lag between these bands reveals the distance between the optical and γ -ray emission regions. Jet precession can be induced by mechanisms such as a binary black hole system (J. I. Katz 1997) or Lense–Thirring (LT) precession (J. Lense & H. Thirring 1918).

Considering the jet precession model, relativistic jet precessing goes around an axis and forms a conical surface with a precession angle Ω . The cone axis forms an angle Φ_0 with the direction of the line of sight and has a projected angle η_0 on the plane of sky (e.g. S. Britzen et al. 2018). The time-dependent viewing angel (θ) and the position angle (η) can be expressed by

$$\eta(t) = \arctan \frac{y}{r} \tag{14}$$

$$\theta(t) = \arcsin\left(\sqrt{x^2 + y^2}\right),\tag{15}$$

with

$$x = A(t)\cos \eta_0 - B(t)\sin \eta_0$$
, $y = A(t)\sin \eta_0 + B(t)\cos \eta_0$, (16)

and

$$A(t) = \cos \Omega \sin \Phi_0 + \sin \Omega \sin \omega (t - T_0) \cos \Phi_0, B(t)$$

= \sin \O \cos \omega(t - T_0), (17)

where $\omega=2\pi/P_{\rm obs}$ is the angular velocity. The changing Doppler factor is obtained by $\delta=\Gamma\left(1-\beta\cos\theta(t)\right)^{-1}$, where $\Gamma=(1-\beta^2)^{-\frac{1}{2}}$ is the bulk Lorentz factor and $\beta=v_{\rm jet}/c$ is the bulk velocity. Substituting above equations into $F=\delta^3F'$, we can obtain the varying observed flux due to the jet precession,

$$F(t) = \frac{F'}{\Gamma^3 \left[1 - \beta \cos \left(\arcsin \sqrt{x^2 + y^2} \right) \right]^3}.$$
 (18)

The term η_0 is completely cancelled out in equation (18), indicating that η_0 does not affect our result. We modelled the observed light curve with the period of $P_{\rm obs} = 609.7$ d, as shown in Fig. 8.

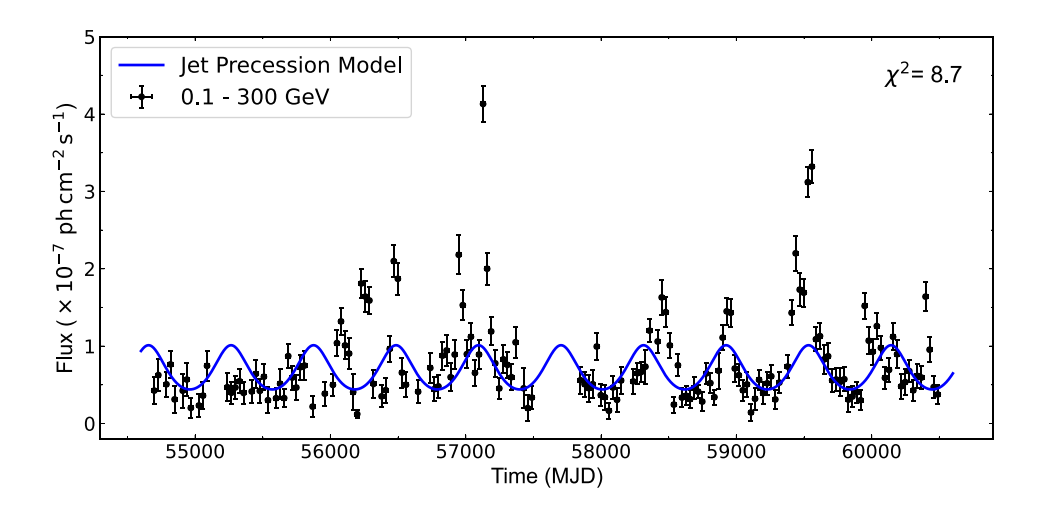


Figure 8. The fitting jet precession model. The solid line represents the results of the precessing jet model.

The light curve is well fitted by the jet precession model with the χ^2 value between the model and the data as 8.7. The best-fitting parameters are determined as follows: $\Omega=2.0^\circ\pm0.6^\circ$, $\Phi_0=5.3^\circ\pm1.2^\circ$, $\Gamma=5.1\pm0.6$, $F'=(11.6\pm3.0)\times10^{-11}$ ph cm⁻² s⁻¹, $T_0=55417.9\pm6.1$. Our fitting results are reasonable, as Φ_0 typically fluctuates by a few degrees, and previous studies have found the mean Doppler factor for FSRQs to be around 10 (J.-H. Fan et al. 2009; T. Hovatta et al. 2009; I. Liodakis et al. 2018).

5 CONCLUSION

In this work, we report the detection of a OPO in the γ -ray band (0.1-300 GeV) of 4FGL J0309.9-6058 using ~16 yr of Fermi-LAT observations. Through applying three Fourier-based timeseries analysis methods, LSP, REDDIT, and WWZ, we consistently identified a QPO signal with a mean period of approximately 550 d. Specifically, the LSP yielded a period of 561.29 ± 74.15 d with a local significance of 3.47 σ and a global significance of 2.30 σ ; REDFIT indicated a period of 548.15 \pm 83.04 d with a significance exceeding 99 per cent; and the WWZ method revealed a period of 552.00 \pm 65.66 d with a local significance of 3.72σ and a global significance of 2.72σ . In addition, GP modelling independently produced a bestfitting period of 560.66 d, consistent with the results obtained from Fourier-based methods. We further extended our analysis to the full duration of the Fermi observations, and the results consistently support the OPO signal, strengthening the reliability of our detection. Additionally, we extended the QPO investigation to the optical band and found similar QPO behavior using ATLAS data. However, more optical observations are necessary to firmly establish the QPO signal in that band. In addition, we detected a time lag of 228 d between the optical and γ -ray bands, suggesting the separated emission regions for optical and γ -ray emissions. Considering the year-like time-scale of the detected QPO and the time lag, we suggest that jet precession is the most plausible physical mechanism responsible for the QPO behavior for 4FGL J0309.9-6058.

ACKNOWLEDGEMENTS

HBX acknowledges the support from the National Natural Science Foundation of China (NSFC 12203034), the Shanghai Science and Technology Fund (22YF1431500), the science research grants

from the China Manned Space Project (CMS-CSST-2025-A07), and the Shanghai Municipal Education Commission regarding artificial intelligence empowered research. SHZ acknowledges support from the National Natural Science Foundation of China (Grant No. 12173026), the National Key Research and Development Program of China (Grant No. 2022YFC2807303), the Shanghai Science and Technology Fund (Grant No. 23010503900), the Program for Professor of Special Appointment (Eastern Scholar) at Shanghai Institutions of Higher Learning and the Shuguang Program (23SG39) of the Shanghai Education Development Foundation and Shanghai Municipal Education Commission. JHF acknowledges the support from the National Natural Science Foundation of China (NSFC U2031201), National Natural Science Foundation of China (NSFC 11733001), National Natural Science Foundation of China (NSFC 12433004), the Scientific and Technological Cooperation Projects (2020-2023) between the People's Republic of China and the Republic of Bulgaria, the science research grants from the China Manned Space Project with No. CMS-CSST-2021-A06, and the support for Astrophysics Key Subjects of Guangdong Province and Guangzhou City. This research was partially supported by the Bulgarian National Science Fund of the Ministry of Education and Science under grants KP-06-H38/4 (2019), KP-06-KITAJ/2 (2020), and KP-06-H68/4 (2022).

DATA AVAILABILITY

The data presented in this article will be shared on reasonable request to the corresponding author.

REFERENCES

Abdo A. A. et al., 2010, ApJ, 716, 30 Abdollahi S. et al., 2020, ApJS, 247, 33 Abdollahi S. et al., 2022, ApJS, 260, 53 Abraham Z., Carrara E. A., 1998, ApJ, 496, 172 Abraham Z., Romero G. E., 1999, A&A, 344, 61 Accadia T. et al., 2012, J. Instrum., 7, 3012 Ackermann M. et al., 2015, ApJ, 813, L41 Agazie G. et al., 2023a, ApJ, 951, L9 Agazie G. et al., 2023b, ApJ, 951, L10 Atwood W. B. et al., 2009, ApJ, 697, 1071 Baluev R. V., 2008, MNRAS, 385, 1279

```
Banerjee A., Sharma A., Mandal A., Das A. K., Bhatta G., Bose D., 2023, MNRAS, 523, L52
```

Bassa C., Wang Z., Cumming A., Kaspi V. M., eds, 2008, AIP Conf. Ser. Vol. 983, 40 Years of Pulsars: Millisecond Pulsars, Magnetars and More. Am. Inst. Phys., New York

Bell M. E. et al., 2011, MNRAS, 411, 402

Bhatta G., 2019, MNRAS, 487, 3990

Bhatta G., Dhital N., 2020, ApJ, 891, 120

Blandford R. D., Koenigl A., 1979, Astrophys. Lett., 20, 15

Britzen S. et al., 2018, MNRAS, 478, 3199

Camenzind M., Krockenberger M., 1992, A&A, 255, 59

Celotti A., Padovani P., Ghisellini G., 1997, MNRAS, 286, 415

Chakrabarti S. K., Wiita P. J., 1993, ApJ, 411, 602

Chalumeau A. et al., 2022, MNRAS, 509, 5538

Chatterjee R. et al., 2008, ApJ, 689, 79

Chen J., Yu J., Huang W., Ding N., 2024, MNRAS, 528, 6807

Connolly S. D., 2016, Astrophysics Source Code Library, record ascl:1602.012

Dong F.-T., Gai N., Tang Y., Wang Y.-F., Yi T.-F., 2022, Res. Astron. Astrophys., 22, 115001

Edelson R. A., Krolik J. H., 1988, ApJ, 333, 646

Emmanoulopoulos D., McHardy I. M., Papadakis I. E., 2013, MNRAS, 433, 907

Fan J.-H., Huang Y., He T.-M., Yang J. H., Hua T. X., Liu Y., Wang Y. X., 2009, PASJ, 61, 639

Fan J.-H., Liu Y., Qian B.-C., Tao J., Shen Z.-Q., Zhang J.-S., Huang Y., Wang J., 2010, Res. Astron. Astrophys., 10, 1100

Fan J. H., Kurtanidze O., Liu Y., Richter G. M., Chanishvili R., Yuan Y. H., 2014, ApJS, 213, 26

Fan J. H. et al., 2016, ApJS, 226, 20

Fan J. H. et al., 2018, AJ, 155, 90

Fan J. H. et al., 2021, ApJS, 253, 10

Fermi Science Support Development Team, 2019, Astrophysics Source Code Library, record ascl:1905.011

Foreman-Mackey D., Agol E., Ambikasaran S., Angus R., 2017, AJ, 154, 220

Foster G., 1996, AJ, 112, 1709

Ghisellini G., Tavecchio F., 2008, MNRAS, 387, 1669

Ghisellini G., Tavecchio F., 2009, MNRAS, 397, 985

Horne J. H., Baliunas S. L., 1986, ApJ, 302, 757

Hovatta T., Valtaoja E., Tornikoski M., Lähteenmäki A., 2009, A&A, 494, 527

Huang C.-Y., Wang D.-X., Wang J.-Z., Wang Z.-Y., 2013, Res. Astron. Astrophys., 13, 705

Jenet F. et al., 2009, preprint (arXiv:0909.1058)

Katz J. I., 1997, ApJ, 478, 527

Lee K. J., 2016, in Qain L., Li D., eds, ASP Conf. Ser. Vol. 502, Frontiers in Radio Astronomy and FAST Early Sciences Symposium 2015. Astron. Soc. Pac., San Francisco, p. 19

Lehto H. J., Valtonen M. J., 1996, ApJ, 460, 207

Lense J., Thirring H., 1918, Physikalische Zeitschrift, 19, 156

Li H.-Z., Gao Q.-G., Qin L.-H., Yi T.-F., Chen Q.-R., 2022, Res. Astron. Astrophys., 22, 055017

Li X.-P., Luo Y.-H., Yang H.-Y., Yang C., Cai Y., Yang H.-T., 2017, ApJ, 847, 8

Li X.-P., Yang H.-Y., Cai Y., Song X.-F., Yang H.-T., Shan Y.-Q., 2023, Res. Astron. Astrophys., 23, 095010

LIGO Scientific Collaboration, 2015, Class. Quantum Gravity, 32, 074001

Liodakis I., Hovatta T., Huppenkothen D., Kiehlmann S., Max-Moerbeck W., Readhead A. C. S., 2018, ApJ, 866, 137

Lomb N. R., 1976, Ap&SS, 39, 447

Lynden-Bell D., 1969, Nature, 223, 690

Maggiore M., 2007, Gravitational Waves, vol. 1: Theory and Experiments.
Oxford Univ. Press, Oxford

Manchester R. N., IPTA, 2013, Class. Quantum Gravity, 30, 224010

Mangalam A. V., Wiita P. J., 1993, ApJ, 406, 420

Max-Moerbeck W., Richards J. L., Hovatta T., Pavlidou V., Pearson T. J., Readhead A. C. S., 2014, MNRAS, 445, 437

Mücke A., Protheroe R. J., 2001, Astropart. Phys., 15, 121

O'Neill S. et al., 2022, ApJ, 926, L35

Otero-Santos J. et al., 2020, MNRAS, 492, 5524

Ouyang Z. et al., 2025, ApJ, 980, 19

Padovani P., 2017, Front. Astron. Space Sci., 4, 35

Planck Collaboration VI, 2020, A&A, 641, A6

Prokhorov D. A., Moraghan A., 2017, MNRAS, 471, 3036

Qian S.-J. et al., 2007, Chinese J. Astron. Astrophys., 7, 364

Rani B., Wiita P. J., Gupta A. C., 2009, ApJ, 696, 2170

Rieger F. M., 2004, ApJ, 615, L5

Salpeter E. E., 1964, ApJ, 140, 796

Sandrinelli A., Covino S., Dotti M., Treves A., 2016, AJ, 151, 54

Scargle J. D., 1982, ApJ, 263, 835

Schramm K. J. et al., 1993, A&A, 278, 391

Schulz M., Mudelsee M., 2002, Comput. Geosci., 28, 421

Sesana A., 2013, MNRAS, 433, L1

Shapiro S. S., Wilk M. B., 1965, Biometrika, 52, 591

Shaw M. S. et al., 2012, ApJ, 748, 49

Sillanpaa A., Haarala S., Valtonen M. J., Sundelius B., Byrd G. G., 1988, ApJ, 325, 628

Smith K. W. et al., 2020, PASP, 132, 085002

Spiewak R. et al., 2022, PASA, 39, e027

Timmer J., König M., 1995, A&A, 300, 707

Tonry J. L. et al., 2018a, PASP, 130, 064505

Tonry J. L. et al., 2018b, ApJ, 867, 105

Urry C. M., Padovani P., 1995, PASP, 107, 803

Uttley P., McHardy I. M., Papadakis I. E., 2002, MNRAS, 332, 231

Uttley P., McHardy I. M., Vaughan S., 2005, MNRAS, 359, 345

Valtonen M. J. et al., 2006, ApJ, 646, 36

Villata M., Raiteri C. M., Sillanpaa A., Takalo L. O., 1998, MNRAS, 293, L.13

Wang G. G., Cai J. T., Fan J. H., 2022, ApJ, 929, 130

Xiao H.-B. et al., 2024, Res. Astron. Astrophys., 24, 065013

Xu H. et al., 2023, Res. Astron. Astrophys., 23, 075024

Zhang H., Yan D., Zhang P., Yang S., Zhang L., 2021, ApJ, 919, 58

Zhang H., Wu F., Dai B., 2023, PASP, 135, 064102

Zhang L., Chen X., He S., Nie W., Tang W., Huang J., Chen G., Fan J., 2024, ApJS, 271, 27

Zhang P.-f., Yan D.-h., Liao N.-h., Wang J.-c., 2017, ApJ, 835, 260

Zhou J., Wang Z., Chen L., Wiita P. J., Vadakkumthani J., Morrell N., Zhang P., Zhang J., 2018, Nat. Commun., 9, 4599

APPENDIX

The posterior distributions of parameters for the Gaussian Process are shown in Fig. A1.

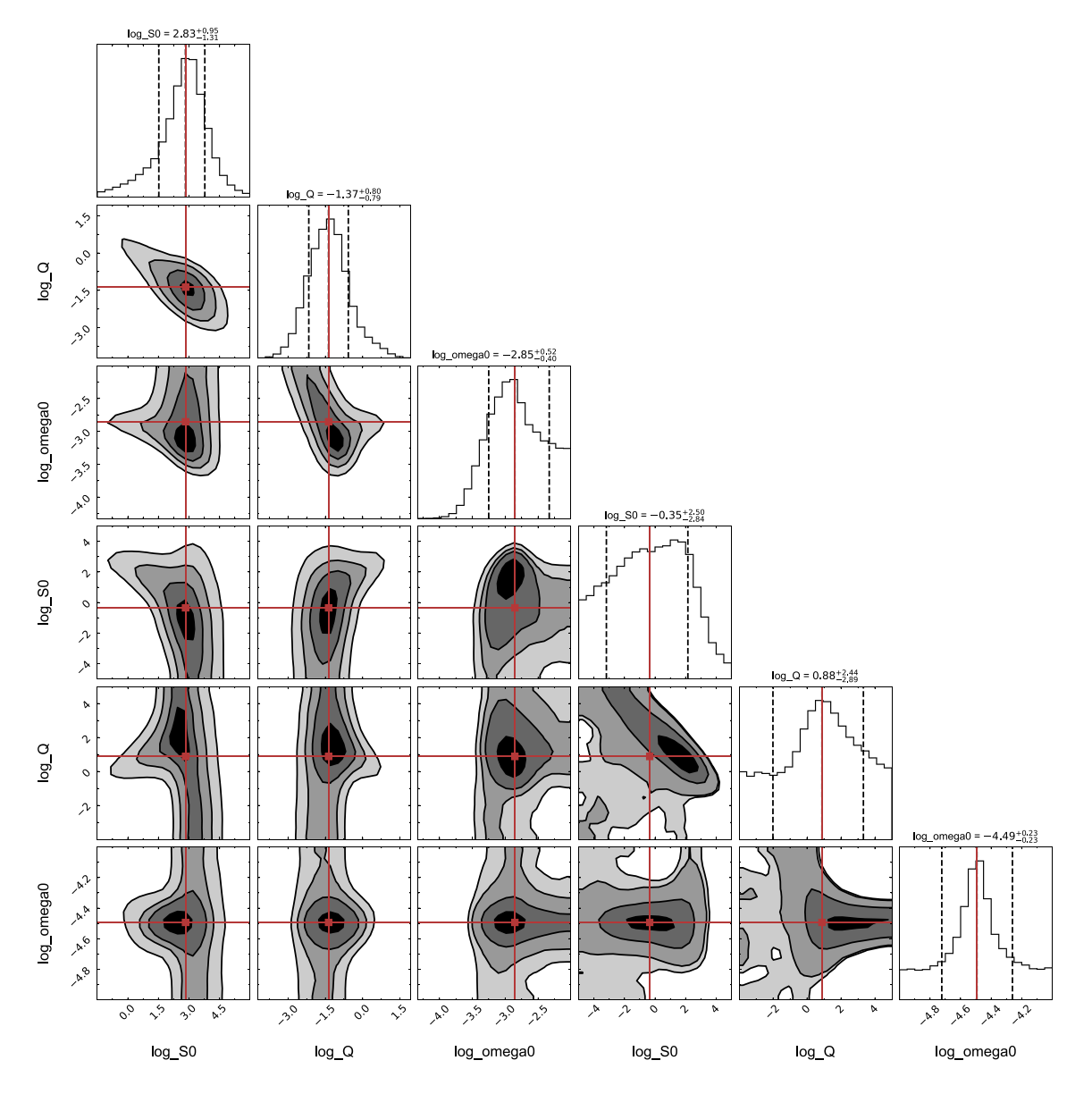


Figure A1. Posterior distributions from the MCMC analysis for the Gaussian Process with SHO \times 2 model. The best-fitting values are taken from the 50th percentiles, as shown by the solid lines, and the associated uncertainties correspond to the 16th and 84th percentiles.

This paper has been typeset from a TEX/IATEX file prepared by the author.